actuators

Article

Mechanical Property Degradation of Entangled Metallic Wire Materials under Vibration Environment: Experiments and Prediction Models

Yanhong Ma [1], Tianyu Liang [2], Yongfeng Wang [2,*], Zhizhou Wang [1] and Jie Hong [2]

[1] Research Institute of Aero-Engine, Beihang University, Beijing 100191, China
[2] School of Energy and Power Engineering, Beihang University, Beijing 100191, China
* Correspondence: wangyongfeng@buaa.edu.cn

Abstract: Entangled metallic wire material (EMWM) can be utilized as a novel elastic element in vibration isolation devices for mechanical actuators. This paper presents a vibration experiment aimed at investigating the degradation behavior of mechanical performance in EMWM under a cyclic compressive environment. An electric vibration testing system, coupled with an isolation structure, is employed to apply compressive loads to the EMWM specimens. Through visual observations and quasi-static compression tests, the variations in geometric morphology and mechanical properties are studied, considering different relative densities and vibrational stress amplitudes. The results indicate a significant reduction in the compressed dimension of the specimens as the number of cycles increases, without any wire fractures or wear. The mechanical properties exhibit an increasing secant modulus and a decreasing loss factor. These variations ultimately lead to a gradual deviation of the vibration characteristics of the isolation structure from its design state, including resonance frequency and transmission rate. To forecast the mechanical property degradation of EMWM, prediction models are proposed, incorporating its dimensions, modulus, and damping by fitting the experiment results. This research provides valuable experimental data and presents an effective method to determine the operational lifespan of vibration isolators utilizing EMWM.

Keywords: entangled metallic wire material; vibration experiment; cyclic compressive loads; mechanical property degradation; prediction model

Citation: Ma, Y.; Liang, T.; Wang, Y.; Wang, Z.; Hong, J. Mechanical Property Degradation of Entangled Metallic Wire Materials under Vibration Environment: Experiments and Prediction Models. *Actuators* **2023**, *12*, 418. https://doi.org/10.3390/act12110418

Academic Editor: Giorgio Olmi

Received: 27 September 2023
Revised: 6 November 2023
Accepted: 7 November 2023
Published: 8 November 2023

1. Introduction

The external actuators of aerospace crafts and submersibles are subjected to continuous, severe fluid and mechanical excitations, where thin-walled components are prone to vibration fatigue failure [1,2]. To address this issue, it is common to design vibration isolation devices to reduce the stress and deformation of the actuators. In some demanding engineering vibration environments, traditional silicone rubber isolators exhibit drawbacks such as poor tolerance to high and low temperatures and susceptibility to aging [3,4]. Entangled metallic wire material (EMWM) is a functional porous material produced through the winding, stretching, weaving, molding, and post-processing of metallic wires. Some researchers have developed elastic elements in isolators using EMWM as a substitute for silicone rubber [5,6]. Within its structures, numerous metallic wires interlock, connect, and mesh together, creating a significant volume of voids [7–9]. When subjected to compressive loads, the metallic wires undergo bending deformation, resulting in relative deformation and dry friction between the wires. This unique behavior imparts excellent elastic (Young's modulus between 0.1 and 50 MPa) and damping properties (loss factor between 0.12 and 0.26) to EMWM due to its relative density [10–12]. With its notable advantages, such as high- and low-temperature resistance, corrosion resistance, radiation resistance, and the ability to tailor its mechanical properties through process parameters, EMWM offers a broader range of engineering applications compared to traditional rubber materials.

For instance, researchers have successfully utilized EMWM in areas such as vibration isolation and damping [13,14], energy absorption [15–17], sound absorption and noise reduction [18,19], and biomedical implants [20,21]. In these applications, EMWM is often employed as a replaceable component that requires periodic replacement. However, the determination of EMWM's service lifetime lacks established design criteria, and currently, failure is typically recognized only when changes in its mechanical properties are observed through experiments.

To address the issues of damage, failure, and durability of EMWM in engineering applications, extensive research has been conducted [22–25]. For instance, under high-amplitude tensile and compressive cyclic loads, EMWM primarily experiences wire wear and fatigue failure, resulting in the generation of significant amounts of debris and broken wires observed after experiments. Scanning electron microscopy reveals evident abrasion marks and fracture surfaces on the internal surfaces of the metallic wires. Under torsional loading, EMWM undergoes hardening, and the combined action of normal and shear stresses leads to 45-degree cracking in the specimens [26]. Under sustained static loads, the contact status of the internal metallic wires in EMWM undergoes changes, leading to alterations in macroscopic geometric dimensions and mechanical properties. If the strain values induced by the static load are small (less than 10% strain), EMWM does not experience mechanical failure [27].

The application of EMWM in the field of vibration isolation involves the design of various isolator configurations [28,29]. These isolators aim to significantly reduce vibration transmission rates by adjusting the natural frequency of the isolated system through the flexible support provided by elastic components. Due to the cold-press forming process, the tensile and shear strengths of EMWM are generally low, making it suitable for withstanding compressive cyclic loads [30,31]. Currently, the dynamic characteristics of EMWM isolators have been studied by many researchers [32,33]. However, there are limited studies on the degradation behavior of the mechanical property and the expected lifespan of EMWM.

This paper presents an innovative exploration of the degradation behavior of the mechanical properties of EMWM under cyclic compressive loads by using a typical vibration isolation structure. The mechanical properties are analyzed through dimension measurements and quasi-static compression tests. Prediction models are developed that accurately forecast the mechanical property degradation of EMWM, considering key factors such as its geometric dimensions, modulus, and loss factor. This research provides valuable insights into EMWM's mechanical behaviors and a robust methodology for determining the operational lifespan of isolators. The organization of this paper comprises six sections. Section 1 is the introduction, providing an overview of the research. Section 2 briefly introduces the EMWM specimens employed in the experiment. Section 3 introduces the methods of the vibration experiment and the quasi-static compression test. Section 4 presents the experimental results and discussions, encompassing the variations in vibration characteristics of the isolation structure, geometries, secant modulus, and loss factor of the EMWM specimens. In Section 5, prediction models for property degradation, aimed at predicting operational lifespan, are presented. These models are developed through the fitting of experimental data. Section 6 concludes this paper, summarizing the degradation behavior of EMWM under a vibration environment and addressing the research's limitations.

2. Material and Specimens

The metallic wires used in the production of EMWM were supplied by Anping Risheng Wire Mesh Ltd., in Hengshui, China. These wires are made of stainless steel, specifically the grade 0Cr18Ni9. The manufacturing process of EMWM specimens followed the procedures illustrated in Figure 1. Initially, the metallic wires were tightly wound to form closely spaced helixes using a wire winding machine. Subsequently, the helixes were stretched into spiral coils according to the pitch parameter. These coils were then woven together manually to create a blank. Finally, the blank was cold-pressed into EMWM specimens of the desired shape using molds and a press machine.

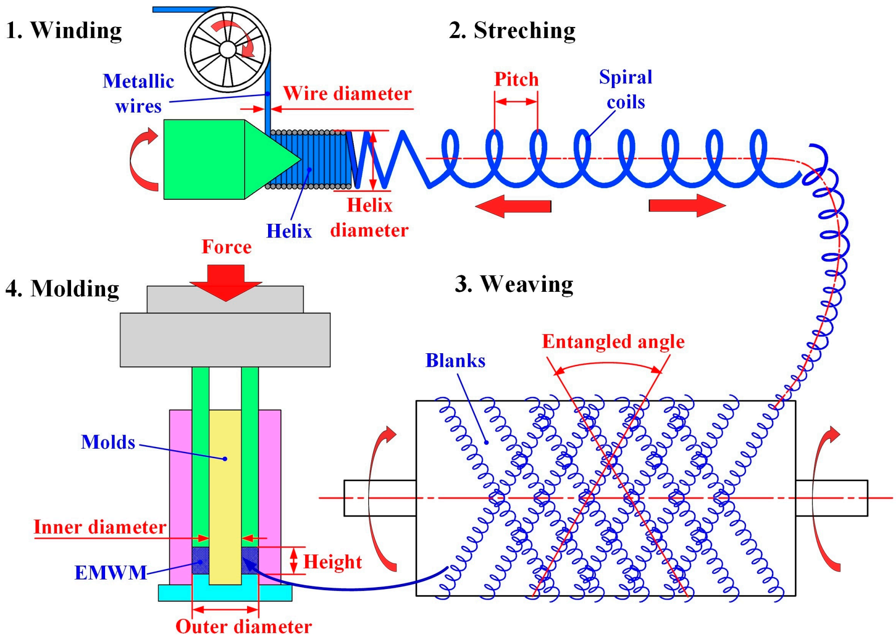

Figure 1. The manufacturing procedures of EMWM.

To maintain the geometrical characteristics typically applied in vibration isolators, the EMWM specimens in the experiments were manufactured into a hollow cylindrical shape with an outer diameter of 37 mm, an inner diameter of 18 mm, and a height of 15 mm, as illustrated in Figure 2. These EMWM specimens were designed to be representative of the mechanical characteristics due to their nominal size being more than 10 times the helix diameter. These dimensions allow the specimens to accommodate a significant number of coiled wires and minimize the influence of boundary layers.

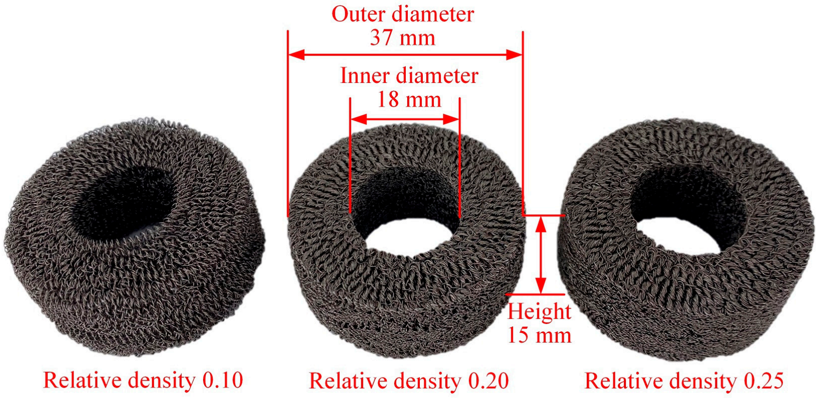

Figure 2. The geometric parameters of EMWM specimens.

In the vibration experiment, several pairs of EMWM specimens were tested to investigate the influence of different relative densities and stress amplitudes on mechanical property degradation. The manufacturing parameters used for the EMWM specimens are presented in Table 1. Relative density is a controlled parameter in the manufacturing process, and its actual value exhibits minimal deviations, which can be ignored in engineering applications. A pair of specimens (labeled with a pair number) was utilized in a single vibration experiment, and three pairs of specimens were manufactured with the same set of parameters to minimize random errors. Specimens A1-3, B1-3, and C1-3 were employed to investigate the influence of relative density. Specimens C1-3, D1-3, and E1-3, with the same set of parameters, were used to investigate the influence of vibrational stress amplitude.

Table 1. The manufacturing parameters of the EMWM specimens.

Pair Number	Wire Diameter (mm)	Helix Diameter (mm)	Pitch (mm)	Relative Density	Forming Pressure (MPa)	Inner Diameter (mm)	Outer Diameter (mm)	Height (mm)	Mass (g)
A1	0.10	1.1	1.1	0.10	11.57	17.97	37.04	15.11	9.73
A2	0.10	1.1	1.1	0.10	11.57	17.86	37.01	15.15	9.71
A3	0.10	1.1	1.1	0.10	11.57	17.93	37.05	15.20	9.71
B1	0.10	1.1	1.1	0.20	29.85	17.99	37.08	15.14	19.47
B2	0.10	1.1	1.1	0.20	29.85	18.00	37.08	15.05	19.47
B3	0.10	1.1	1.1	0.20	29.85	17.89	37.05	15.10	19.46
C1	0.10	1.1	1.1	0.25	48.74	17.92	37.06	15.13	24.30
C2	0.10	1.1	1.1	0.25	48.74	17.84	37.02	15.05	24.34
C3	0.10	1.1	1.1	0.25	48.74	17.92	37.02	15.25	24.31
D1	0.10	1.1	1.1	0.25	48.74	17.92	37.01	15.14	24.31
D2	0.10	1.1	1.1	0.25	48.74	17.99	37.00	15.14	24.34
D3	0.10	1.1	1.1	0.25	48.74	17.87	37.04	15.22	24.30
E1	0.10	1.1	1.1	0.25	48.74	18.00	37.05	15.04	24.32
E2	0.10	1.1	1.1	0.25	48.74	17.94	37.05	15.12	24.31
E3	0.10	1.1	1.1	0.25	48.74	17.91	37.02	15.25	24.31

Relative density, ρ_r, is a critical design parameter that significantly affects the mechanical properties of EMWM. It quantifies the volume fraction of coiled wires within the entire specimen and is defined by Equation (1). Some studies also uses the term "porosity" to describe the porous characteristics of EMWM.

$$\rho_r = \frac{\rho_{EMWM}}{\rho_{wire}} = \frac{M}{\rho_{wire} V} \tag{1}$$

where ρ_{EMWM} represents the actual density of EMWM. ρ_{wire} represents the density of the metallic wire material. M and V represent the mass and volume of the specimen, respectively. Stress amplitude, S, as described in the following section, Section 3.1, is a mechanical parameter utilized in the vibration experiment.

3. Experimental Methods

3.1. Vibration Experiment of the Isolation Structure

A vibration isolation structure was designed to replicate the working conditions of general isolators to subject the EMWM specimens to an identical vibration environment, as illustrated in Figure 3a. A pair of EMWM specimens with the same parameters set were tested within the isolation structure. The components of the isolation structure, from top to bottom, included a mass block, threaded rod, upper plate, specimen 1, middle plate, specimen 2, lower plate, and base. The installation of an EMWM specimen onto the threaded rod and plate is illustrated in Figure 3b. An auxiliary tool was used to align the central axis of the specimen with the threaded rod. During the installation process, the threaded rod and nut were tightened to achieve an initial compression deformation of the EMWM specimens. Thread adhesive was used to securely fasten the threaded rod and nut, preventing any loosening during the vibration experiment. The initial deformation was set at 0.5 mm, controlled by the distance between the upper plate and the lower plate. The isolation structure maintained the EMWM specimens in a compressed state throughout the vibration experiment, consistent with the stress state in a general isolator. When the mass block induced a downward displacement relative to the threaded rod, the upper specimen (specimen 1) underwent compression. When the mass block induced an upward displacement, the lower specimen (specimen 2) underwent compression.

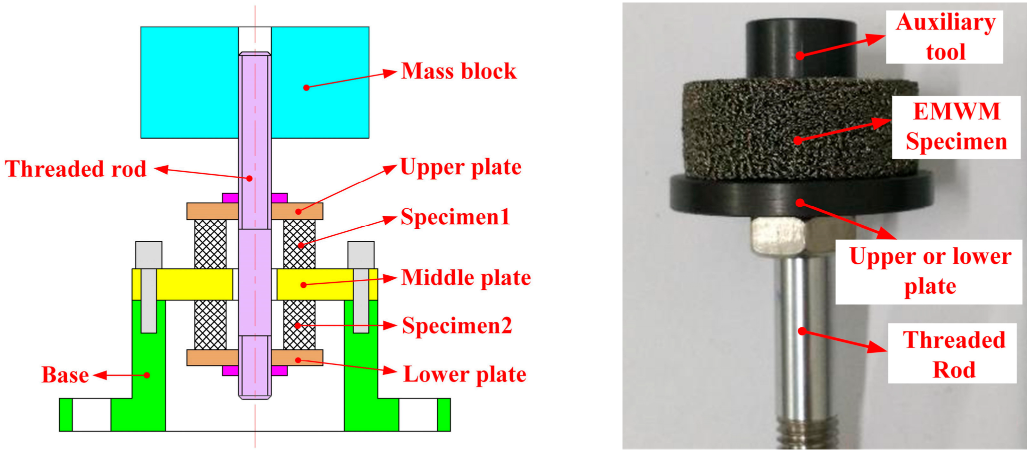

(**a**) (**b**)

Figure 3. (**a**) The vibration isolation structure used to install a pair of EMWM specimens; (**b**) Installation of an EMWM specimen onto the threaded rod and plate.

The vibration experiments were conducted using the DC-1000-15/SV-0606 electric vibration testing system provided by Sushi Experimental Instrument Co., Ltd., Suzhou, China. The experimental setup for the vibration experiment is illustrated in Figure 4. The isolation structure was mounted on the vertical vibration platform using four bolts. Two accelerometers were employed to capture the vibration excitation signal and response signal of the isolation structure. Accelerometer 1 was attached to the vibration platform. Accelerometer 2 was attached to the top of the mass block. The platform generated vertical vibrations, and the frequency and amplitude were controlled by a computer.

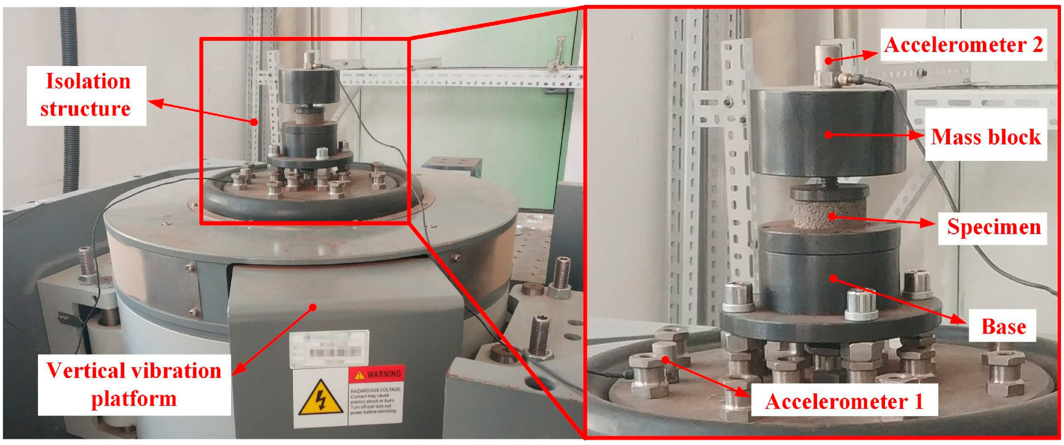

Figure 4. The vibration experiment setup, including the electric vibration testing system and the isolation structure of EMWM specimens.

The isolation structure can be simplified as a single-degree-of-freedom vibration system, as illustrated in Figure 5a. In the case where the specimens are continuously compressed during the experiment, each specimen can be individually modeled as a spring and a damper. The motion equation for this model can be expressed as Equation (2). If the two EMWM specimens are identical, we can set $k_1 = k_2 = k$ and $c_1 = c_2 = c$. Consequently, the compression cycles in the vibration experiment were conducted using a stress-controlling method, and the compressive force, $F(t)$, exerted on each EMWM specimen was calculated using Equation (3).

$$m\ddot{u}_2(t) + (c_1 + c_2)\big(\dot{u}_2(t) - \dot{u}_1(t)\big) + (k_1 + k_2)(u_2(t) - u_1(t)) = 0 \tag{2}$$

$$F(t) = k(u_2(t) - u_1(t)) + c(\dot{u}_2(t) - \dot{u}_1(t)) = -\frac{1}{2}m\ddot{u}_2(t) \tag{3}$$

where m represents the mass of the mass block. $\ddot{u}_1(t)$ and $\ddot{u}_2(t)$ represent the acceleration of the vibration platform and the mass block, respectively, as measured by the accelerometers. k_1 and k_2 represent the stiffness of the EMWM specimens. c_1 and c_2 represent the viscous damping coefficient. The compressive load applied to each specimen should also include the preloading force, F_0, exerted by the threaded rod and nut. As a result, the stress, $\sigma(t)$, and stress amplitude, S, on each specimen during the compression cycles are calculated using Equation (4).

$$\sigma(t) = (F_0 + F(t))/A, S = \max(\sigma(t)) \tag{4}$$

where A represents the cross-sectional area of the EMWM specimen. As both specimens were exclusively designed to endure compressive forces in both the initial and operational states, the EMWM specimens underwent sinusoidal compression cycles, as illustrated in Figure 5b.

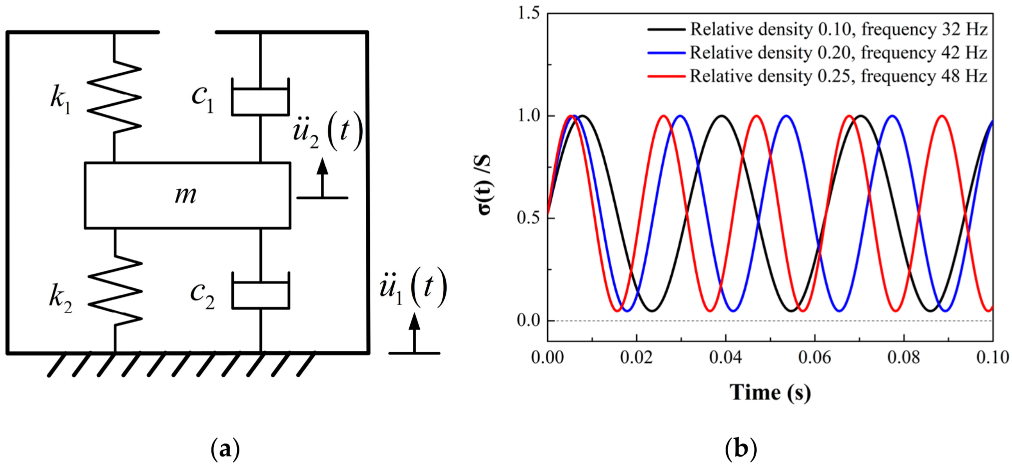

Figure 5. (**a**) Dynamic model of the vibration isolation structure; (**b**) the sinusoidal compression cycles applied on the EMWM specimens.

Before the vibration experiment on the EMWM specimens, the frequency–response characteristics curve of the isolation structure was measured using accelerometers, as illustrated in Figure 6. The resonance frequencies for the EMWM specimens with relative densities of 0.10, 0.20, and 0.25 were determined to be 32 Hz, 42 Hz, and 48 Hz, respectively. In the vibration experiment, sinusoidal compression cycles were applied to the EMWM specimens at 40 Hz in the sub-resonance region to expedite the experiment. The sub-resonance region was determined using the half-power bandwidth method, depicted by the magenta areas in Figure 6. Three different excitation amplitudes were applied to the isolation structure by controlling the vibration amplitudes of the electric vibration testing system. Compressive stress amplitudes of 0.3 MPa, 0.7 MPa, and 1.0 MPa were calculated using Equations (3) and (4). After a specified number of compression cycles, the isolation structure was disassembled. The dimensions of the EMWM specimes were then measured using a vernier caliper. The measurement of the mechanical properties, including secant modulus and loss factor, was conducted using quasi-static compression tests. The measurements of the dimensions and mechanical properties were taken at intervals of 10^6 compression cycles during the vibration experiment, for a total of 10^7 cycles.

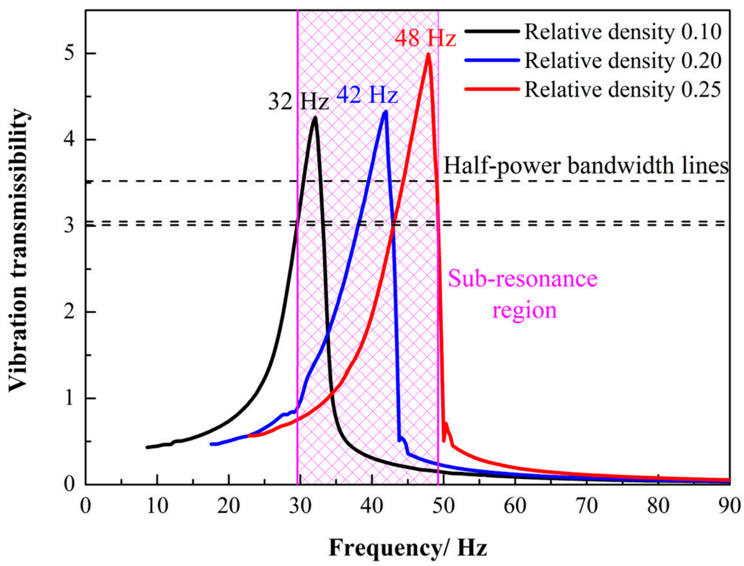

Figure 6. The frequency–response characteristics curve of the vibration isolation structure.

3.2. Quasi-Static Compression Test

The quasi-static compression tests were conducted using a WDW3100 microcomputer-controlled electronic universal testing machine provided by Changchun Kexin Experimental Instrument Co., Ltd., Changchun, China. The experimental setup consisted of a force sensor, dial gauge, pressure plate, and base, as illustrated in Figure 7. Prior to and following the vibration experiments of the isolation structure, quasi-static compression tests were performed with a maximum compressive force of 100 N to evaluate the variations in modulus and damping after a specified number of cyclic loads.

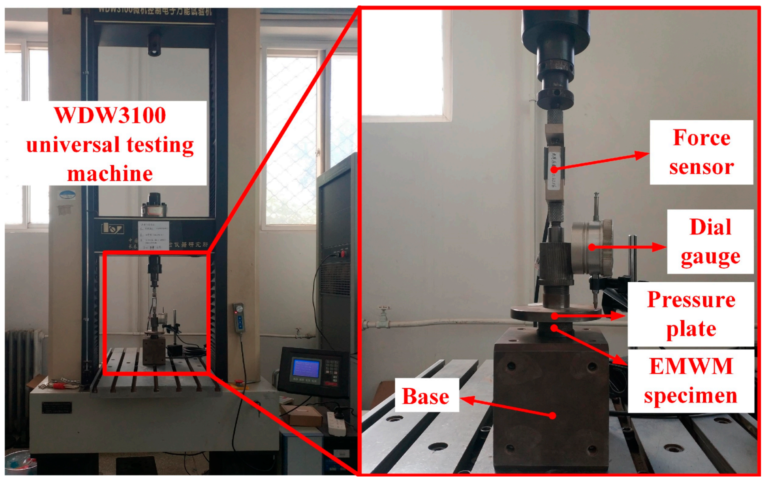

Figure 7. The experimental setup of the quasi-static compression test.

At low compressive forces (e.g., 100 N, as employed in this work), the compression strain is small and the stress–strain relationship of EMWM remains in the linear phase. The elastic property of EMWM is described using the secant modulus, E_s, which is defined as follows:

$$E_s = \frac{\Delta\sigma}{\Delta\varepsilon} = \frac{\Delta F/A}{\Delta L/L} \tag{5}$$

where $\Delta\sigma$ represents the stress variation. $\Delta\varepsilon$ represents the strain variation. ΔF represents the maximum compressive force. A represents the cross-sectional area of the specimen. ΔL represents the maximum compression deformation. L represents the initial height of the specimen.

Due to the friction and irreversible deformation between the internal metallic wires, the stress–strain curves during the loading and unloading of EMWM do not coincide, resulting in a hysteresis loop, as illustrated in Figure 8.

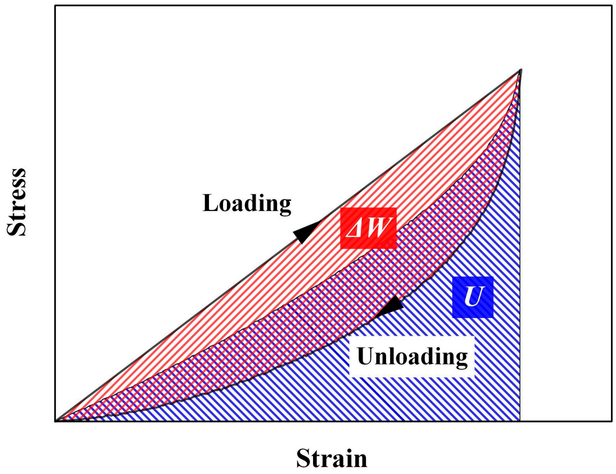

Figure 8. Schematic stress–strain curves of quasi-static compression.

The damping property of a dynamic system with energy dissipation can be quantified using the loss factor, η, defined by Equation (6). It represents the damping performance of EMWM.

$$\eta = \frac{\Delta W}{\pi U} \tag{6}$$

where ΔW represents the dissipated energy, illustrated as the area enclosed by the loading and unloading curves (red-shaded region in Figure 8). U represents the maximum elastic potential energy, illustrated as the projected area of the midline of the loading and unloading curves (blue shaded region in Figure 8). Since a pair of EMWM specimens were tested simultaneously in each vibration experiment, the final results of secant modulus and loss factor were averaged for the two specimens.

4. Results and Discussion

4.1. Vibration Characteristics of Isolation Structure

After a certain number of compression cycles, the resonant frequency and transmission rate at the resonance of the isolation structure were measured through frequency sweep experiments. The transmission rate, tr, was calculated using the acceleration parameters illustrated in Figure 5a, according to the following equation:

$$tr = \ddot{u}_2(t)/\ddot{u}_1(t) \tag{7}$$

where $\ddot{u}_1(t)$ and $\ddot{u}_2(t)$ represent the acceleration of the vibration platform and the mass block, respectively. The results indicate that the resonant frequency and transmission rate of the isolation structure decrease with an increasing number of compression cycles. These observations are illustrated in Figures 9 and 10, respectively. It is noteworthy that the EMWM specimens with lower relative densities exhibit a more rapid deviation of the isolation structure from its designed mechanical performance, consequently shortening the operational lifetime.

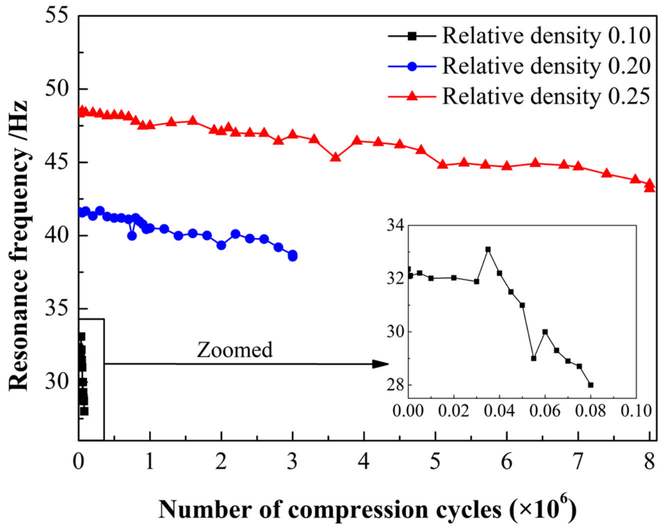

Figure 9. Resonance frequency of isolation structure with specimens of different relative densities.

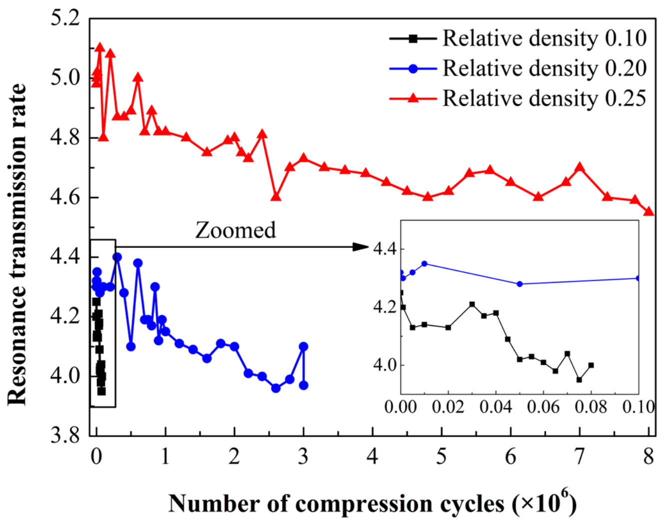

Figure 10. Resonance transmission rate of isolation structure with specimens of different relative densities.

4.2. Geometries and Dimensions

Following the completion of the compression cycles, the EMWM specimens were extracted from the isolation structure to visually inspect their geometric and morphological features. The appearance of the EMWM specimens with different relative densities after 10^7 compression cycles is shown in Figure 11. The specimens retained their cylindrical shape, with minimal alterations in their cross-sectional dimensions. No fractures or significant wear of the metallic wires were observed on the surface of the EMWM specimens. However, a noticeable decrease in height along the compression direction was evident, accompanied by the occurrence of gaps within the isolation structure. This finding indicates that the vibration environment induces irreversible deformation in the compression direction of the EMWM specimens.

Additionally, computed tomography (CT) scanning was performed on the specimens to generate their three-dimensional structure, as shown in Figure 12. The continuity of the metallic wires within the EMWM specimens was confirmed using the contact search algorithm described in Reference [34], and no wire fractures were detected. This finding suggests that the primary failure mode of the EMWM was irreversible deformation in the compression direction rather than the fracture, fatigue, or wear of the metallic wires.

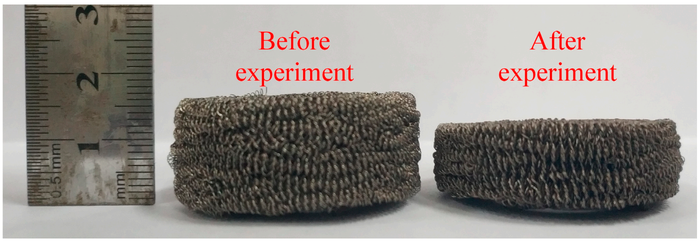

(**a**)

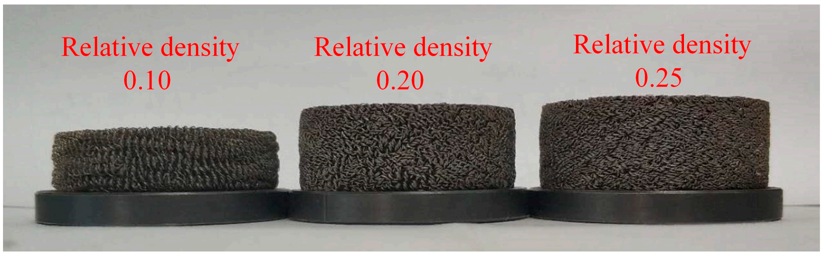

(**b**)

Figure 11. Visual appearance of specimens after the vibration experiment: (**a**) specimen A3 and (**b**) specimens with different relative densities.

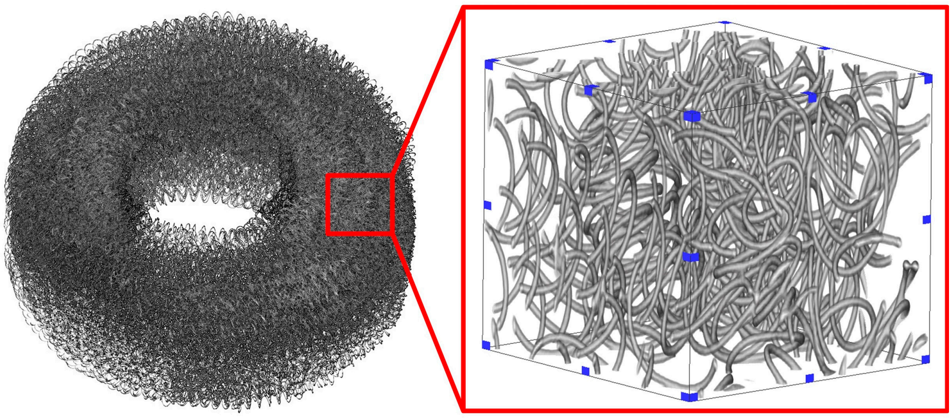

Figure 12. The three-dimensional structure of specimen A3, obtained through CT scanning.

The influence of the relative density and stress amplitude on the variation in specimen height is illustrated in Figure 13. It is evident that increasing the relative density leads to a decrease in height deformation, while increasing the stress amplitude results in an increase in specimen height reduction.

To facilitate the normalized description of the height variation in EMWM specimens, the height variation rate, ψ_h, is defined as follows:

$$\psi_h = (h_N - h_0)/h_0 \tag{8}$$

where h_0 represents the initial height of the EMWM specimen. h_N represents the height after N compression cycles. The height variation rates for different relative densities and stress amplitudes are illustrated in Figure 14. The shape of these curves can be approximated as a bilinear function. Initially, the height variation rate exhibits a rapid increase with the number of compression cycles until it reaches a specific threshold value. Subsequently, the rate of increase in the height variation rate significantly slows down or remains nearly constant.

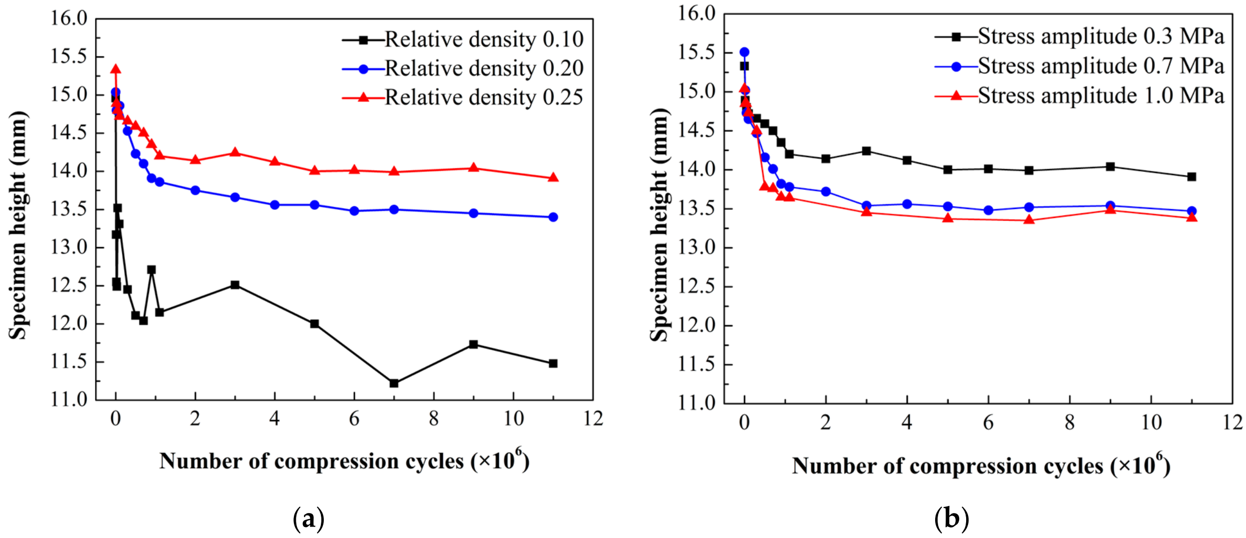

Figure 13. The variation in specimen height: (**a**) for different relative densities with a stress amplitude of 0.3 MPa, (**b**) with a relative density of 0.25 under different stress amplitudes.

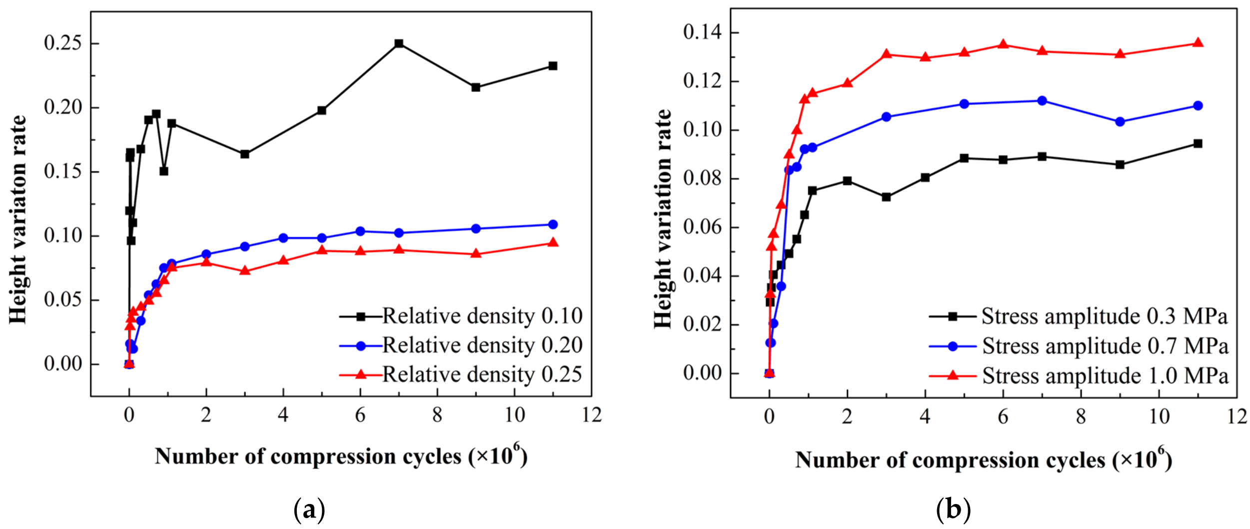

Figure 14. The height variation rates of specimens: (**a**) for different relative densities and (**b**) under different compressive stress amplitudes.

4.3. Quasi-Static Mechanical Properties

Following the dimensional measurements, quasi-static compression tests were conducted to determine the mechanical properties of the EMWM specimens, including the secant modulus and loss factor. The maximum compressive stress applied to the specimens was maintained at 0.3 MPa, aligning with the practical load conditions experienced by isolators. The compression process was almost exclusively confined within the linear elastic range of EMWM. Multiple measurements were conducted for each state, and the mechanical properties of the EMWM specimens exhibited remarkable consistency. The stress–strain curves after the last vibrational compression cycle are illustrated in Figure 15. The influences of the relative density and compressive stress amplitude are investigated to enhance EMWM's feasibility for engineering applications.

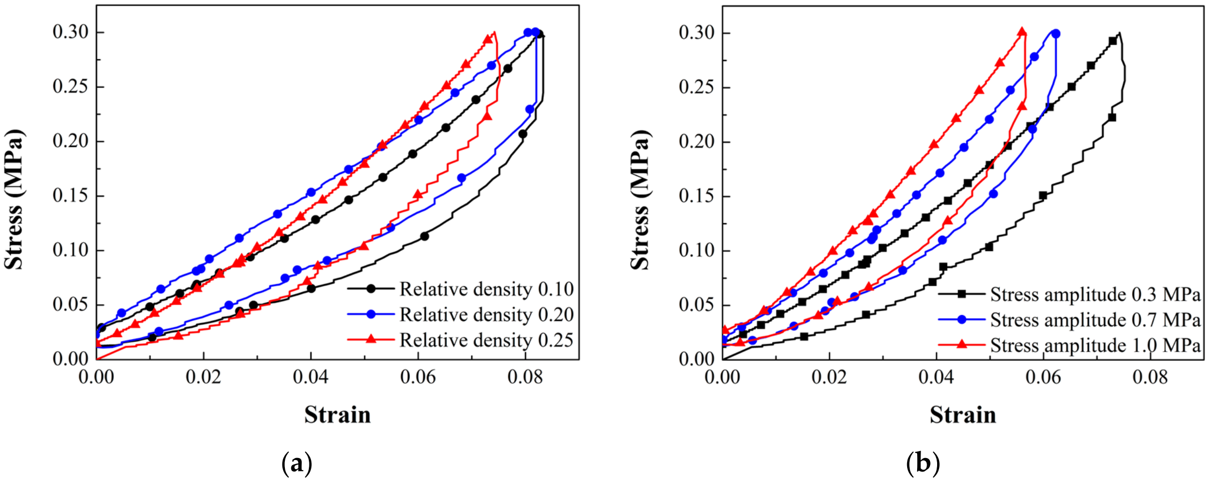

Figure 15. The stress–strain curves obtained by quasi-static compression tests: (**a**) EMWM specimens with different relative densities, specimens A1, B1, and C1, (**b**) EMWM specimens with different stress amplitudes, specimens C1, D1, and E1.

4.3.1. Secant Modulus

The secant modulus of the EMWM specimens, tested under a compressive force of 100 N, after a specified number of compression cycles is presented in Figure 16. The results indicate a significant increase in the secant modulus with an increasing number of compression cycles. However, once the cycle number reaches a threshold value of approximately 10^6, the secant modulus stabilizes at a relatively constant level. It is noteworthy that the EMWM specimens with different relative densities exhibit different initial secant modulus values. However, after undergoing a sufficient number of compression cycles, their secant moduli converge and become nearly equal. Furthermore, when subjected to higher compressive stress amplitudes, both the stabilizated secant modulus and its rate of change during the initial stage exhibit larger values.

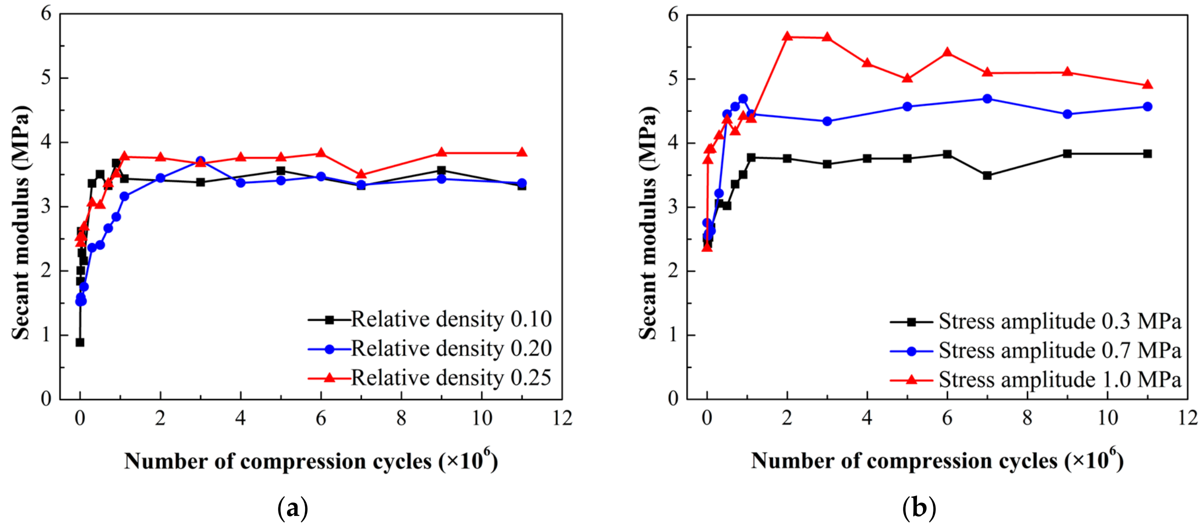

Figure 16. The variation in secant modulus: (**a**) for different relative densities at a stress amplitude of 0.3 MPa and (**b**) at a relative density of 0.25 under different stress amplitudes.

Considering the differences in the initial secant modulus, the variation in the secant modulus in EMWM specimens can be described using a normalized approach. The modulus variation rate, ψ_E, is defined as follows:

$$\psi_E = (E_{s,N} - E_{s,0})/E_{s,0} \tag{9}$$

where $E_{s,0}$ represents the initial secant modulus of the EMWM specimen. $E_{s,N}$ represents the secant modulus after N compression cycles. The modulus variation rates for different relative densities and stress amplitudes are presented in Figure 17. Compared to Figure 16a, the values of the stabilized modulus variation rate in Figure 17a exhibit varying levels for the EMWM specimens with different relative densities. Additionally, an approximate bilinear function can also be observed from these figures.

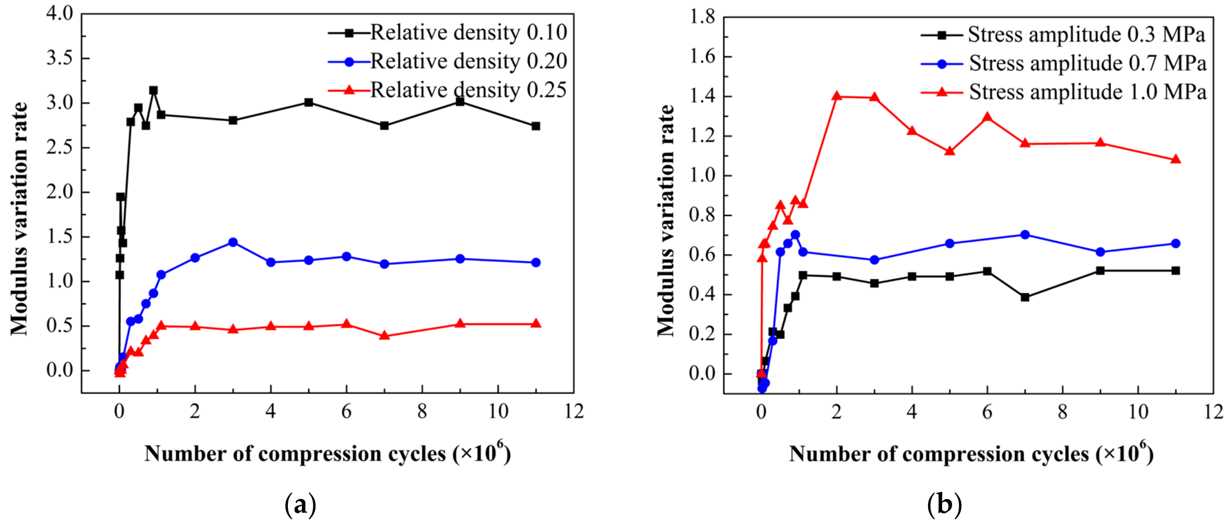

Figure 17. The modulus variation rates of specimens: (**a**) for different relative densities and (**b**) under different compressive stress amplitudes.

4.3.2. Loss Factor

The loss factors of the EMWM specimens after a specified number of compression cycles are presented in Figure 18. The results indicate a significant decrease in the loss factor with an increasing number of compression cycles. However, once the cycle number reaches a threshold value of approximately 10^6, the rate of decrease slows down and eventually stabilizing within a range of 0.13–0.18. It is noteworthy that the EMWM specimens with higher relative densities exhibit a lower initial and stabilized loss factor. Furthermore, when subjected to higher compressive stress amplitudes, the loss factor decreases at a faster rate and reaches a smaller value after stabilization.

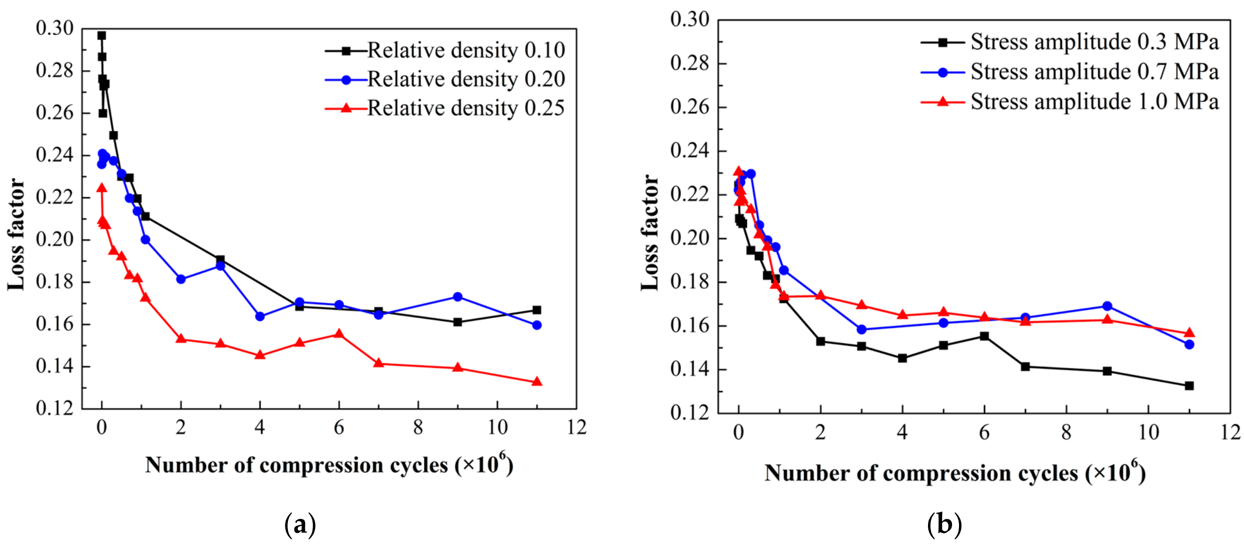

Figure 18. The variation in loss factor: (**a**) for different relative densities at a stress amplitude of 0.3 MPa and (**b**) at a relative density of 0.25 under different stress amplitudes.

Similar to the secant modulus, the variation in the loss factor in the EMWM specimens can be described using a normalized approach. The damping variation rate, ψ_η, is defined as follows:

$$\psi_\eta = (\eta_N - \eta_0)/\eta_0 \tag{10}$$

where η_0 represents the initial loss factor of the EMWM specimen. η_N represents the loss factor after N compression cycles. The damping variation rates for different relative densities and stress amplitudes are presented in Figure 19. The increase in the speed of the damping variation rate gradually decreases with the number of compression cycles, resulting in an approximate polynomial function shape of the curves.

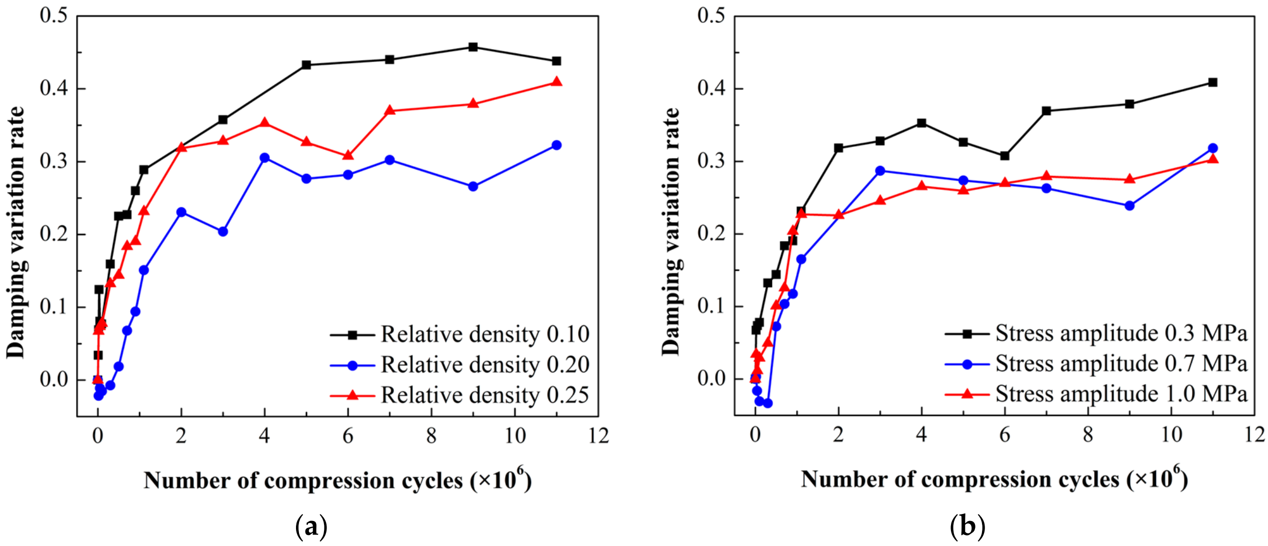

Figure 19. The damping variation rate of the specimens (**a**) for different relative densities and (**b**) under different compressive stress amplitudes.

4.4. Discussion of the Parameter Variations

As illustrated in Figure 20, the scanning electron microscope images of the EMWM reveal that the contact states between internal metallic wires can be classified as non-contact, sliding contact, and adhesive contact. When subjected to compression loads, the contact states among metallic wires transition from non-contact to sliding contact and gradually evolve into adhesive contact, resulting in an increased number of contact points within the EMWM. The progression of contact points is substantiated by the numerical simulation results in Reference [35].

In the cyclic compression vibration tests, variations in the dimensions and quasi-static mechanical properties of the EMWM can be reasonably explicated by the transformations in the contact states of the metallic wires. Under cyclic compression loads, the non-contact metallic wires in the EMWM can enter the sliding state, leading to deformation in the direction of compression. Depending on the positions of the contact points, the sliding state transitions into an adhesive state, which remains irrecoverable upon unloading the compression force, resulting in macroscopic geometric deformations of the EMWM. Conversely, the transition from sliding to adhesive states increases the internal constraints of the metallic wires, culminating in their enhanced resistance to deformation, specifically, an increased modulus. Furthermore, an increase in the number of contact points in the adhesive state amplifies the resistance of metallic wires undergoing micro-sliding, leading to a decreased loss factor in the EMWM.

The increase in relative density results in more contact points within the EMWM, particularly in the adhesive state. Under identical compression loads, the occurrence of relative sliding deformation between the metallic wires becomes more challenging, resulting in reduced alterations in their geometric dimensions and moduli.

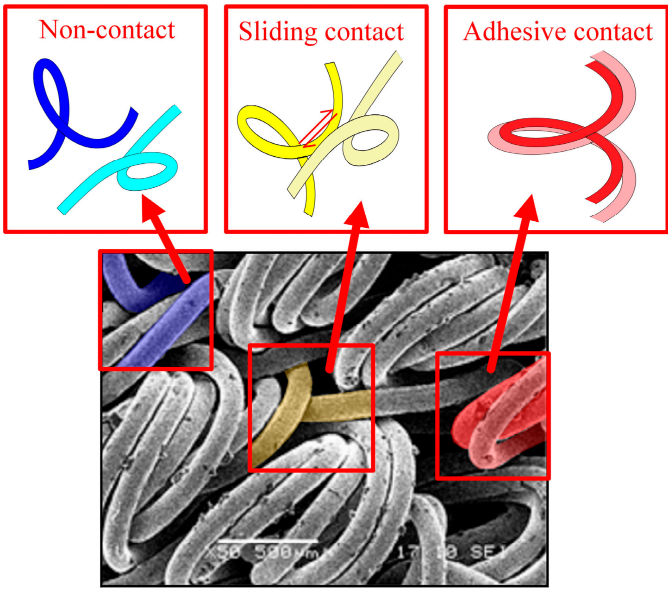

Figure 20. The scanning electron microscope images of the EMWM.

The increase in the vibration stress amplitude induces a larger deformation of the EMWM during compression, with more contact points transitioning to the adhesive state and remaining irrecoverable. Consequently, the changes in the geometric dimensions and modulus of the EMWM experience a significant increase.

The experimental data presented reveal that the variations in the dimensions, modulus, and loss factor of the EMWM predominantly occur during the initial stages of the compression cycles, typically within approximately 10^6 cycles. When EMWM is directly integrated into isolators to provide stiffness and damping, it will result in changes in their natural frequencies and a decline in their isolation performance in a relatively short period. As a consequence, it is very important to enhance the stability of the mechanical properties of EMWM in a vibrational environment for its application in isolators.

5. Prediction Models of Property Degradation

We have proposed a post-processing technique for EMWM, referred to as "vibration training". Before being integrated into isolators, the EMWM undergoes vibrational compression cycles within an equivalent isolator structure. Following the vibration treatment, the EMWM exhibits a remarkable reduction in variations in geometric dimensions, modulus, and loss factor during its practical application within isolators.

In this section, prediction models for geometric dimensions, modulus, and damping are presented to anticipate the degradation of EMWM properties under a compressive vibration environment in support of this technique. These models employ the rate of property variations derived from the vibration experiments and fit them to mathematical formulas.

5.1. Dimension Prediction Model

The experimental results presented in Figure 14 indicate that the curves of height variation rate exhibit an approximately linear segment and a plateau segment with an increasing number of compression cycles. These observations can be effectively described by employing a bilinear mathematical model to predict the height of EMWM specimens. A threshold value is introduced as the pivotal point, with the corresponding number of compression cycles being approximately 10^6. Hence, the fundamental expression of the dimension prediction model can be formulated as follows:

$$\begin{cases} \psi_h = bN,\ 0 \le N \le N_h^0 \\ \psi_h = \psi_h^0,\ N_h^0 \le N \end{cases} \tag{11}$$

where ψ_h represents the height variation rate of the specimen. N represents the number of compression cycles. b represents the slope of the linear segment. ψ_h^0 represents the threshold value. N_h^0 represents the number of compression cycles of the threshold value, close to 10^6.

When $0 \leq N \leq 10^6$, a linear fitting method is employed to fit the experimental data of height variation rates. The slopes, b, corresponding to different combinations of relative densities and stress amplitudes are obtained, as present in Table 2.

Table 2. The slope, b, for the linear segment of height variation rate.

Number	**Relative Density** ρ_r	**Stress Amplitude** S **(MPa)**	**Slope** b
1	0.10	0.3	0.2450
2	0.20	0.3	0.0934
3	0.25	0.3	0.0849
4	0.25	0.7	0.1144
5	0.25	1.0	0.1411

These data points (ρ_r, S, b) are used to establish a functional expression for the slope, b. Based on the trends, we assume that the slope, b, has a power function relationship with the relative density, ρ_r, and stress amplitude, S, expressed as follows:

$$b = m_1 \cdot \rho_r^{m_2} \cdot S^{m_3} \tag{12}$$

where m_1, m_2, and m_3 are all fitting coefficients. The values of these fitting coefficients are obtained through the least squares fitting method, resulting in

$$b = 0.03 \times \rho_r^{-1.22} \times S^{0.47} \tag{13}$$

The threshold value, ψ_h^0, can be calculated by averaging the height variation rates, ψ_h, above 10^6 compression cycles, as present in Table 3.

Table 3. The threshold value, ψ_h^0, of height variation rate.

Number	**Relative Density** ρ_r	**Stress Amplitude** S **(MPa)**	**Threshold Value** ψ_h^0
1	0.10	0.3	0.2080
2	0.20	0.3	0.0971
3	0.25	0.3	0.0836
4	0.25	0.7	0.1058
5	0.25	1.0	0.1289

These data points $\left(\rho_r, S, \psi_h^0\right)$ are used to establish a functional expression for the threshold value, ψ_h^0. Based on the trends, we assume that the threshold value, ψ_h^0, has a power function relationship with the relative density, ρ_r, and stress amplitude, S, expressed as follows:

$$\psi_h^0 = p_1 \cdot \rho_r^{p_2} \cdot S^{p_3} \tag{14}$$

where p_1, p_2, and p_3 are all fitting coefficients. The values of these fitting coefficients are obtained through the least squares fitting method, resulting in

$$\psi_h^0 = 0.03 \times \rho_r^{-1.03} \times S^{0.37} \tag{15}$$

By combining Equations (11), (13), and (15), we obtain the final dimension prediction model for the EMWM specimens:

$$\begin{cases} \psi_h = bN,\ 0 \leq N \leq N_h^0 \\ \psi_h = \psi_h^0,\ N_h^0 \leq N \\ b = 0.03 \times \rho_r{}^{-1.22} \times S^{0.47} \\ \psi_h^0 = 0.03 \times \rho_r{}^{-1.03} \times S^{0.37} \\ N_h^0 = \psi_h^0 / b \end{cases} \tag{16}$$

where the unit of N is 10^6. The unit of S is MPa.

A comparison between the experimental and fitting results for different relative densities and stress amplitudes is shown in Figure 21. It indicates that the model curves match well with the experimental results, demonstrating that the dimension prediction model can accurately predict the height variation in EMWM in a vibration environment.

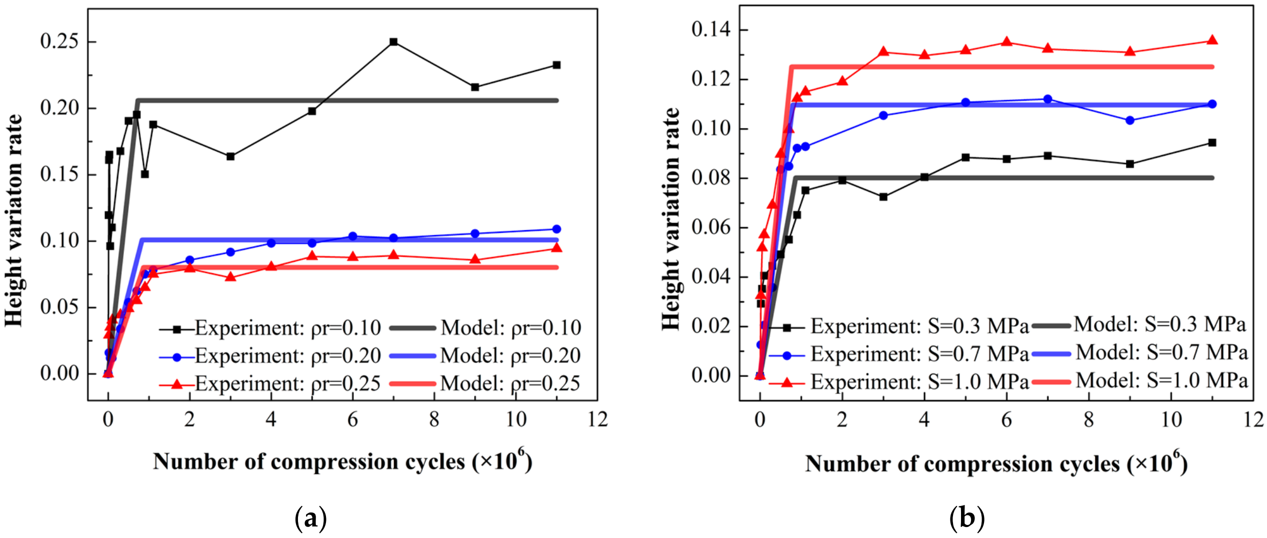

Figure 21. Comparison between the dimension prediction model and experimental results: (**a**) for different relative densities and (**b**) under different compressive stress amplitudes.

5.2. Modulus Prediction Model

The experimental results presented in Figure 17 indicate that the trend of secant modulus variation is similar to that of height. Therefore, the same bilinear mathematical model is used to formulate the modulus prediction model. The fundamental expression is as follows:

$$\begin{cases} \psi_E = cN, 0 \leq N \leq N_E^0 \\ \psi_E = \psi_E^0, N_E^0 \leq N \end{cases} \tag{17}$$

where ψ_E represents the modulus variation rate of the specimen. N represents the number of compression cycles. c represents the slope of the linear segment. ψ_E^0 represents the threshold value. N_E^0 represents the number of compression cycles of the threshold value, close to 10^6.

When $0 \leq N \leq 10^6$, a linear fitting method is employed to fit the experimental data of the modulus rate. The slopes, c, corresponding to different combinations of relative densities and stress amplitudes are obtained, as present in Table 4.

Table 4. The slope, c, for the linear segment of modulus variation rate.

Number	Relative Density ρ_r	Stress Amplitude S (MPa)	Slope c
1	0.10	0.3	3.8560
2	0.20	0.3	1.1385
3	0.25	0.3	0.4676
4	0.25	0.7	0.7842
5	0.25	1.0	1.2325

These data points (ρ_r, S, c) are used to establish a functional expression for the slope, c. Based on the trends, we assume that the slope, c, has a power function relationship with the relative density, ρ_r and stress amplitude, S, expressed as follows:

$$c = n_1 \cdot \rho_r^{n_2} \cdot S^{n_3} \tag{18}$$

where n_1, n_2, and n_3 are all fitting coefficients. The values of these fitting coefficients are obtained through the least squares fitting method, resulting in

$$c = 0.05 \times \rho_r^{-2.21} \times S^{0.60} \tag{19}$$

The threshold value, ψ_E^0, can be calculated by averaging the modulus variation rates, ψ_E, above 10^6 compression cycles, as presented in Table 5.

Table 5. The threshold value, ψ_E^0, of modulus variation rate.

Number	Relative Density ρ_r	Stress Amplitude S (MPa)	Threshold Value ψ_E^0
1	0.10	0.3	2.8639
2	0.20	0.3	1.2417
3	0.25	0.3	0.4860
4	0.25	0.7	0.6374
5	0.25	1.0	1.1874

These data points (ρ_r, S, ψ_E^0) are used to establish a functional expression for the threshold value, ψ_E^0. Based on the trends, we assume that the threshold value, ψ_E^0, has a power function relationship with the relative density, ρ_r, and stress amplitude, S, expressed as follows:

$$\psi_E^0 = q_1 \cdot \rho_r^{q_2} \cdot S^{q_3} \tag{20}$$

where q_1, q_2, and q_3 are all fitting coefficients. The values of these fitting coefficients are obtained through the least squares fitting method, resulting in

$$\psi_E^0 = 0.08 \times \rho_r^{-1.83} \times S^{0.43} \tag{21}$$

By combining Equations (17), (19), and (21), we obtain the final dimension prediction model for the EMWM specimens:

$$\begin{cases} \psi_E = cN,\ 0 \le N \le N_E^0 \\ \psi_E = \psi_E^0,\ N_E^0 \le N \\ c = 0.05 \times {\rho_r}^{-2.21} \times S^{0.60} \\ \psi_E^0 = 0.08 \times {\rho_r}^{-1.83} \times S^{0.43} \\ N_E^0 = \psi_E^0 / c \end{cases} \tag{22}$$

where the unit of N is 10^6. The unit of S is MPa.

A comparison between the experimental and fitting results for different relative densities and stress amplitudes is shown in Figure 22. It indicates that the model curves match well with the experimental results, demonstrating that the modulus prediction model can accurately predict the secant modulus variation of EMWM in a vibration environment.

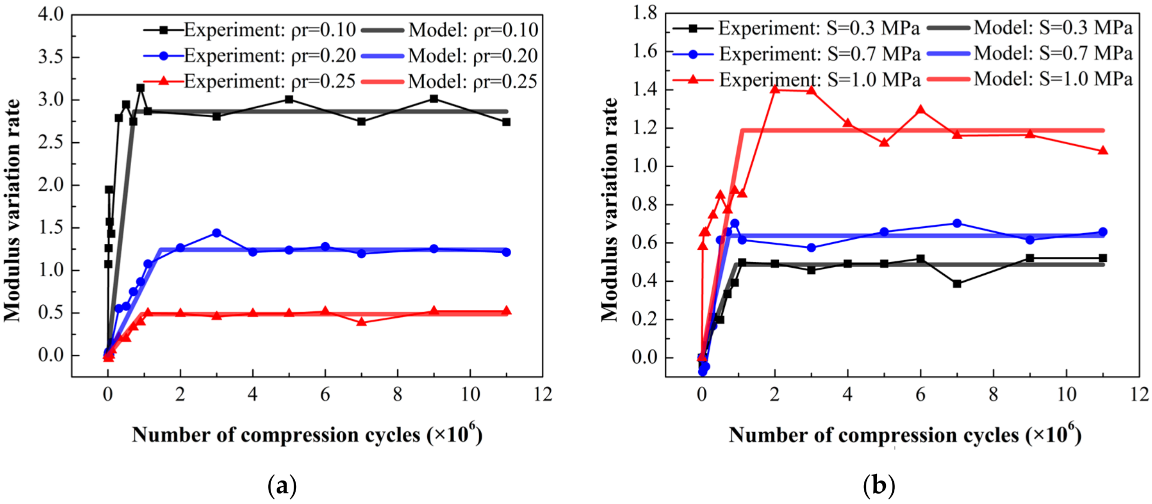

Figure 22. Comparison between the modulus prediction model and experimental results: (**a**) for different relative densities and (**b**) under different compressive stress amplitudes.

5.3. Damping Prediction Model

The experimental results shown in Figure 19 indicate that the curves of the damping variation rate exhibit the charactistics of exponential characteristics with an increasing number of compression cycles. These observations can be effectively described by employing an exponential function model to predict the damping of EMWM specimens. Hence, the fundamental expression of the damping prediction model can be formulated as follows:

$$\psi_\eta = d_1\left(1 - e^{d_2 \cdot N}\right) \tag{23}$$

where ψ_η represents the damping variation rate of the specimen. N represents the number of compression cycles. d_1 and d_2 represent the fitting coefficients. The fitting coefficients, d_1 and d_2, corresponding to different combinations of relative densities and stress amplitudes are obtained, as present in Table 6.

Table 6. The coefficients, d_1 and d_2, of the exponential function.

Number	Relative Density ρ_r	Stress Amplitude S (MPa)	Coefficient d_1	Coefficient d_2
1	0.10	0.3	0.4258	−1.2213
2	0.20	0.3	0.3085	−0.4680
3	0.25	0.3	0.3563	−1.0453
4	0.25	0.7	0.2847	−0.6333
5	0.25	1.0	0.2740	−1.0896

These data points, (ρ_r, S, d_1) and (ρ_r, S, d_2), are used to establish a functional expression for the fitting coefficients d_1 and d_2. Based on the trends, we assume that the fitting coefficients d_1 and d_2 have a power function relationship with the relative density, ρ_r, and stress amplitude, S, expressed as follows:

$$d_1 = s_1 \cdot \rho_r^{s_2} \cdot S^{s_3} \tag{24}$$

$$d_2 = t_1 \cdot \rho_r^{t_2} \cdot S^{t_3} \tag{25}$$

where s_1, s_2, and s_3 are fitting coefficients for d_1. t_1, t_2, and t_3 are fitting coefficients for d_2. The values of these fitting coefficients are obtained through the least squares fitting method, resulting in

$$d_1 = 0.19 \times \rho_r^{-0.26} \times S^{-0.15} \tag{26}$$

$$d_2 = -0.44 \times \rho_r^{-0.52} \times S^{0.25} \tag{27}$$

By combining Equations (23), (26), and (27), we obtain the final damping prediction model for the EMWM specimens:

$$\begin{cases} \psi_\eta = d_1\left(1 - e^{d_2 \cdot N}\right) \\ d_1 = 0.19 \times \rho_r^{-0.26} \times S^{-0.15} \\ d_2 = -0.44 \times \rho_r^{-0.52} \times S^{0.25} \end{cases} \tag{28}$$

where the unit of N is 10^6. The unit of S is MPa.

A comparison between the experimental and fitting results for different relative densities and stress amplitudes is shown in Figure 23. It indicates that the model curves match well with the experimental results, demonstrating that the damping prediction model can accurately predict the loss factor variation of EMWM in a vibration environment.

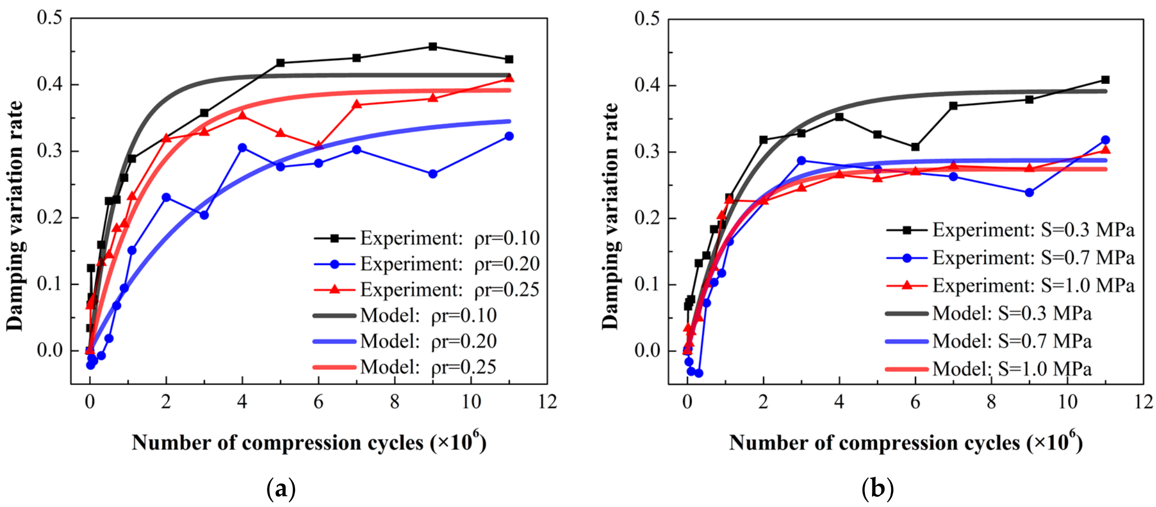

Figure 23. Comparison between the damping prediction model and experimental results: (**a**) for different relative densities and (**b**) under different compressive stress amplitudes.

6. Conclusions

This paper focuses on investigating the degradation behavior of mechanical properties in entangled metallic wire materials (EMWMs) under a compressive vibration environment. A series of experiments was conducted using pairs of EMWM specimens installed in a vibration isolation structure subjected to cyclic compression. The vibration characteristics of the isolation structure are studied using a spectral analysis. The geometric and morphological features of EMWM are examined through visual inspection and CT scanning. The mechanical properties of EMWM are examined through quasi-static compression tests. The main findings and conclusions of this work are listed as follows:

(1) The resonant frequency and transmission rate of the isolation structure showed a clear decrease as the number of compression cycles increased. The mechanical property degradation of EMWM resulted in a deviation from the intended performance of vibration isolators.

(2) The dimension in the compressed direction of the EMWM experienced a noticeable decrease and stabilized when the cycle number reached a certain threshold, approximately 10_6. No wire fractures or significant wear were observed on the surface of or

inside the specimens. The reduction in this dimension may be attributed to changes in the contact status and slight slipping between the internal wires.

(3) The secant modulus exhibited a significant increase, while the loss factor decreased as the number of compression cycles increased. Once the cycle number reached a threshold value of approximately 10_6, these parameters stabilized at relatively constant values. The values of these properties were influenced by the relative density and stress amplitude.

(4) Prediction models for property degradation, including dimensions, modulus, and damping, were developed based on fitting the experimental data. These models can accurately predict the variation in the mechanical properties of EMWM specimens in a vibration environment. If a combination of relative density and cyclic compression stress amplitude is given, the variation in mechanical properties with the number of cycles can be calculated by the prediction models.

(5) Prediction models for property degradation, including dimensions, modulus, and damping, were developed based on fitting the experimental data. These models can accurately predict the variation in the mechanical properties of EMWM specimens in a vibration environment. They provide valuable insights for designing vibration isolators with EMWM and determining their operational lifespan.

Author Contributions: Conceptualization and methodology, Y.M.; methodology, formal analysis, validation, and writing—original draft preparation, T.L.; writing—review and editing, Y.W.; software, investigation, formal analysis, and data curation, Z.W.; supervision, project administration, and funding acquisition, J.H. All authors have read and agreed to the published version of the manuscript.

Funding: This research was funded by the National Natural Science Foundation of China, grant numbers: 52175072 and 52075018.

Data Availability Statement: The data presented in this study are available on request from the corresponding author. The data are not publicly available due to privacy.

Conflicts of Interest: The authors declare no conflict of interest. The funders had no role in the design of the study.

References

1. Guo, H.; Yan, Y.; Xia, H.; Yu, L.; Lv, B. The Prediction and Correction Method of Aircraft Static Aeroelastic Effects: A Review of Recent Progress. *Actuators* **2022**, *11*, 309. [CrossRef]
2. Preumont, A. Active Damping, Vibration Isolation, and Shape Control of Space Structures: A Tutorial. *Actuators* **2023**, *12*, 122. [CrossRef]
3. Fu, J.; Liu, G.; Fan, C.; Liu, Z.; Luo, H. Design and Experimental Study on Vibration Reduction of an UAV Lidar Using Rubber Material. *Actuators* **2022**, *11*, 345. [CrossRef]
4. Ju, S.-H.; Yuantien, C.-C.; Hsieh, W.-K. Study of Lead Rubber Bearings for Vibration Reduction in High-Tech Factories. *Appl. Sci.* **2020**, *10*, 1502. [CrossRef]
5. Chandrasekhar, K.; Rongong, J.; Cross, E. Mechanical behaviour of tangled metal wire devices. *Mech. Syst. Signal Process.* **2019**, *118*, 13–29. [CrossRef]
6. Zhang, B.; Lang, Z.Q.; Billings, S.A.; Tomlinson, G.R.; Rongong, J.A. System identification methods for metal rubber devices. *Mech. Syst. Signal Process.* **2013**, *39*, 207–226. [CrossRef]
7. Ma, Y.; Zhang, Q.; Wang, Y.; Hong, J.; Scarpa, F. Topology and mechanics of metal rubber via X-ray tomography. *Mater. Des.* **2019**, *181*, 108067. [CrossRef]
8. Masse, J.P.; Barbier, C.; Salvo, L.; Brechet, Y.; Bouaziz, O.; Bouvard, D. Mechanical and structural characterization of nonsintered and sintered steel wools by x-ray tomography: Description of the techniques and validation on virtual materials. *J. Mater. Res. Camb. Univ. Press* **2013**, *28*, 2852–2860. [CrossRef]
9. Shlyapin, S.D.; Serov, M.M.; Gusev, D.E.; Fedorova, L.V. Fabrication, Structure, and Properties of Porous Materials Made of Titanium Fibers and Wire. *Russ. J. Non-Ferr. Met.* **2018**, *58*, 670–677. [CrossRef]
10. Gadot, B.; Riu Martinez, O.; Rolland du Roscoat, S.; Bouvard, D.; Rodney, D.; Orgéas, L. Entangled single-wire NiTi material: A porous metal with tunable superelastic and shape memory properties. *Acta Mater.* **2015**, *96*, 311–323. [CrossRef]
11. Rodney, D.; Gadot, B.; Martinez, O.R.; du Roscoat, S.R.; Orgeas, L. Reversible dilatancy in entangled single-wire materials. *Nat. Mater.* **2016**, *15*, 72–77. [CrossRef] [PubMed]

12. Zhang, C.; Ao, H.; Jiang, H. Macro–Microstatic Stiffness Prediction Model of Metal Rubber. *Adv. Theory Simul.* **2021**, *4*, 2100008. [CrossRef]
13. Cao, X.; Wei, C.; Liang, J.; Wang, L. Design and dynamic analysis of metal rubber isolators between satellite and carrier rocket system. *Mech. Sci.* **2019**, *10*, 71–78. [CrossRef]
14. Tang, N.; Rongong, J.A. Feasibility study on the use of tangled metal wire particles as the adjustable elements in tuned mass dampers. *J. Sound Vib.* **2019**, *457*, 1–14. [CrossRef]
15. Zou, Y.; Xiong, C.; Yin, J.; Cui, K.; Zhu, X.; Deng, H.; Song, S.; Poisson, F. Experimental and Constitutive Model Study on Dynamic Mechanical Behavior of Metal Rubber under High-Speed Impact Loading. *Shock. Vib.* **2021**, *2021*, 8845375. [CrossRef]
16. Wu, Y.-W.; Tang, Y.; Li, S.-Z.; Cheng, H.; Chen, X.-C.; Bai, H.-B. Experimental study on the mechanical properties and impact behaviors of entangled metallic wire material under repeated low-velocity impacts. *Mech. Adv. Mater. Struct.* **2022**, *30*, 2506–2516. [CrossRef]
17. Liu, G.; Song, W.; Li, P. Compressive mechanical properties of metal fiber sintered sheets at different strain rates. *Compos. Struct.* **2020**, *233*, 111703. [CrossRef]
18. Guan, D.; Jing, L.; Gong, J.; Shen, H.; Zong, Y. Prediction of sound absorption property of metal rubber using general regression neural network. *Noise Control Eng. J.* **2018**, *66*, 424–431. [CrossRef]
19. Safin, A.I.; Igolkin, A.A.; Prokof'ev, A.B. A mathematical model of acoustic properties of gas turbine engine sound absorbing elements made from elastic porous metal rubber. *Russ. Aeronaut.* **2015**, *57*, 430–434. [CrossRef]
20. He, G.; Liu, P.; Tan, Q. Porous titanium materials with entangled wire structure for load-bearing biomedical applications. *J. Mech. Behav. Biomed. Mater.* **2012**, *5*, 16–31. [CrossRef]
21. Wang, Q.; Qiao, Y.; Cheng, M.; Jiang, G.; He, G.; Chen, Y.; Zhang, X.; Liu, X. Tantalum implanted entangled porous titanium promotes surface osseointegration and bone ingrowth. *Sci. Rep.* **2016**, *6*, 26248. [CrossRef] [PubMed]
22. Lee, M.G.; Lee, K.W.; Hur, H.K.; Kang, K.J. Mechanical behavior of a wire-woven metal under compression. *Compos. Struct.* **2013**, *95*, 264–277. [CrossRef]
23. Lee, M.-G.; Ko, G.-D.; Song, J.; Kang, K.-J. Compressive characteristics of a wire-woven cellular metal. *Mater. Sci. Eng. A* **2012**, *539*, 185–193. [CrossRef]
24. Zhao, Y.; Yan, H.; Wang, Y.; Jiang, T.; Jiang, H. Predicting Nonlinear and Anisotropic Mechanics of Metal Rubber Using a Combination of Constitutive Modeling, Machine Learning, and Finite Element Analysis. *Materials* **2021**, *14*, 5200. [CrossRef]
25. Hu, J.; Du, Q.; Gao, J.; Kang, J.; Guo, B. Compressive mechanical behavior of multiple wire metal rubber. *Mater. Des.* **2018**, *140*, 231–240. [CrossRef]
26. Liu, P.; He, G.; Wu, L. Structure deformation and failure of sintered steel wire mesh under torsion loading. *Mater. Des.* **2009**, *30*, 2264–2268. [CrossRef]
27. Ma, Y.; Zhang, Q.; Zhang, D.; Zhu, H.; Lu, H.; Hong, J. Failure criterion and durability characteristics of metal rubber under static compression load. *J. Beijing Univ. Aeronaut. Astronaut.* **2016**, *42*, 227–235. (In Chinese) [CrossRef]
28. Ertas, B.H. Compliant Hybrid Journal Bearings Using Integral Wire Mesh Dampers. *J. Eng. Gas Turbines Power* **2008**, *131*, 022503. [CrossRef]
29. Ertas, B.; Luo, H.; Hallman, D. Dynamic Characteristics of Shape Memory Alloy Metal Mesh Dampers. In Proceedings of the 50th AIAA/ASME/ASCE/AHS/ASC Structures, Structural Dynamics, and Materials Conference, Palm Springs, CA, USA, 4–7 May 2009. [CrossRef]
30. San Andre's, L.; Chirathadam, T.A.; Kim, T.-H. Measurement of Structural Stiffness and Damping Coefficients in a Metal Mesh Foil Bearing. In Proceedings of the ASME Turbo Expo 2009: Power for Land, Sea, and Air, Orlando, FL, USA, 8–12 June 2009; pp. 763–771. [CrossRef]
31. Kashani, M.M.; Ahmadi, E.; Gonzalez-Buelga, A.; Zhang, D.; Scarpa, F. Layered composite entangled wire materials blocks as pre-tensioned vertebral rocking columns. *Compos. Struct.* **2019**, *214*, 153–163. [CrossRef]
32. Kwon, S.-C.; Jo, M.-S.; Oh, H.-U. Experimental Validation of Fly-Wheel Passive Launch and On-Orbit Vibration Isolation System by Using a Superelastic SMA Mesh Washer Isolator. *Int. J. Aerosp. Eng.* **2017**, *2017*, 5496053. [CrossRef]
33. Zheng, X.; Wang, W.; Wu, Y.; Bai, H. Study of the Dynamic Model and Vibration Performance of Pot-Shaped Metal Rubber. *Materials* **2022**, *15*, 5878. [CrossRef] [PubMed]
34. Ren, Z.; Shen, L.; Huang, Z.; Bai, H.; Shen, D.; Shao, Y. Study on Multi-Point Random Contact Characteristics of Metal Rubber Spiral Mesh Structure. *IEEE Access* **2019**, *7*, 132694–132710. [CrossRef]
35. Ren, Z.; Shen, L.; Bai, H.; Pan, L.; Zhong, S. Constitutive model of disordered grid interpenetrating structure of flexible microporous metal rubber. *Mech. Syst. Signal Process.* **2021**, *154*, 107567. [CrossRef]